Supplementary Information

Tetragonal $CH_3NH_3PbI_3$ is ferroelectric

Yevgeny Rakita[1], Omri Bar-Elli[2], Elena Meirzadeh[1], Hadar Kaslasi[1], Yagel Peleg[1], Gary Hodes[1], Igor Lubomirsky[1], Dan Oron[2], David Ehre[1,a], David Cahen[1,a]

[1] *Materials and Interfaces Dept., Weizmann Institute of Science, 7610001, Rehovot, Israel*

[2] *Physics of Complex Systems Dept., Weizmann Institute of Science, 7610001, Rehovot, Israel*

[a] Electronic mail: david.ehre@weizmann.ac.il ; david.cahen@weizmann.ac.il

Table of Contents:

Section 1*:* *Origins of polarity in perovskites and its detection*

Ionic displacement due to distortion from the ideal cubic perovskite ABX_3 structure is the origin for local or long-range polar nature of perovskites. Perovskites are stacked as corner-sharing [BX_6] octahedrons forming cuboctahedral sites occupied by an *A* cation. A common origin for structural distortion in perovskites is the mismatch between the ionic volume of the different species which make up a unit cell – a mismatch that can be quantified by a ratio of ionic radii, known as Goldschmidt tolerance factor (1). Such imperfection leads to tilting and axial rotation of the relatively rigid corner-sharing octahedra, which lowers the symmetry of the structure (2, 3). As the *A* cation is usually spherically symmetric, tilt and rotation of the [BX_6] octahedron are not enough to form a dipole in a unit cell. Ionic displacements inside the octahedron, however, can lead to polar or anti-polar unit-cells (4, 5). One known chemical origin for ionic displacement in oxide perovskites is the unequal probability of the O^{2-} valence electrons to interact with the orbitals of the non-centrosymmetric *B* valence electrons. This lack of symmetry may create an ionic displacement. In $BaTiO_3$, for example, the interaction between the non-centrosymmetric valence Ti^{4+} *d*-orbital electrons and O^{2-} *p*-orbital electrons cause a small ionic displacement of the Ti^{4+} within the [TiO_6] octahedron, which leads to a polar unit cell and to ferroelectricity (6).

In HaPs, however, the valence orbitals of the *B* group are known (at least for the *p*-block Pb, Sn or Ge) to be mainly *s*-orbitals, which are centrosymmetric (*e.g. 6s* in $MAPbX_3$).(7, 8) Therefore, the chemical origin for spontaneous polarization in $MAPbX_3$ is hypothesized to be sustained by the polar organic group (7). This idea is supported by results from neutron diffraction (9–11), which showed that free rotation of MA^+ create an effectively cubic system (space group: $Pm\bar{3}m$). As the system is cooled down, vibrationally degenerate soft modes of the MA^+ and/or [PbX_6] octahedron are being condensed to a lower degree of degeneracy, meaning that they keep vibrating but with less degenerate modes. This forces the system to take on tetragonal symmetry and by further cooling, a lower degree of degeneracy forces it to become orthorhombic (9).

The reason that a space group notation is omitted after ‘tetragonal’ and ‘orthorhombic’ is due to a confusion that pervades the scientific literature. Based on x-ray- and neutron- diffraction techniques, the tetragonal phase of $MAPbI_3$ (<330 K) was ascribed to a non-polar symmetry space group, *I*4/*mcm*, as well as to a polar one, *I*4*cm* (12). Using Aleksandrov notations for

tilt/displacement notation for perovskite-like systems (5), *I*4/*mcm* and *I*4*cm* have exactly the same octahedron-tilt system, (00ϕ), and the only difference is that *I*4*cm* is also polar along the *c*-direction (having $a = b \neq c$, with a notation for polarity of (00p); cf. Fig. Si for illustration). Following this logic, $MAPbI_3$ can also possess a *Cmca* space group if the polar displacement along the *c*-axis is anti-polar, (00a). The debate regarding the orthorhombic phase (<165 K) is also between a centrosymmetric - *Pnma*, (ϕϕψ)/(000) - and a polar – $Pna2_1$ one with (ϕϕψ)/(0p0)). For $MAPbBr_3$ the debate concerns only the orthorhombic phase (<149 K), similar to what is the case for $MAPbI_3$, where the tetragonal phase (<236 K) was always noted as *I*4/*mcm* (9).

The interpretation of data from diffraction-based techniques depends on the user's choice of the model to which the diffraction pattern should fit. Small deviations, such as between *I*4/*mcm* and *I*4*cm*, can rarely be clearly distinguished, causing disagreements in the literature in oxide perovskites, but not only there (13, 14).

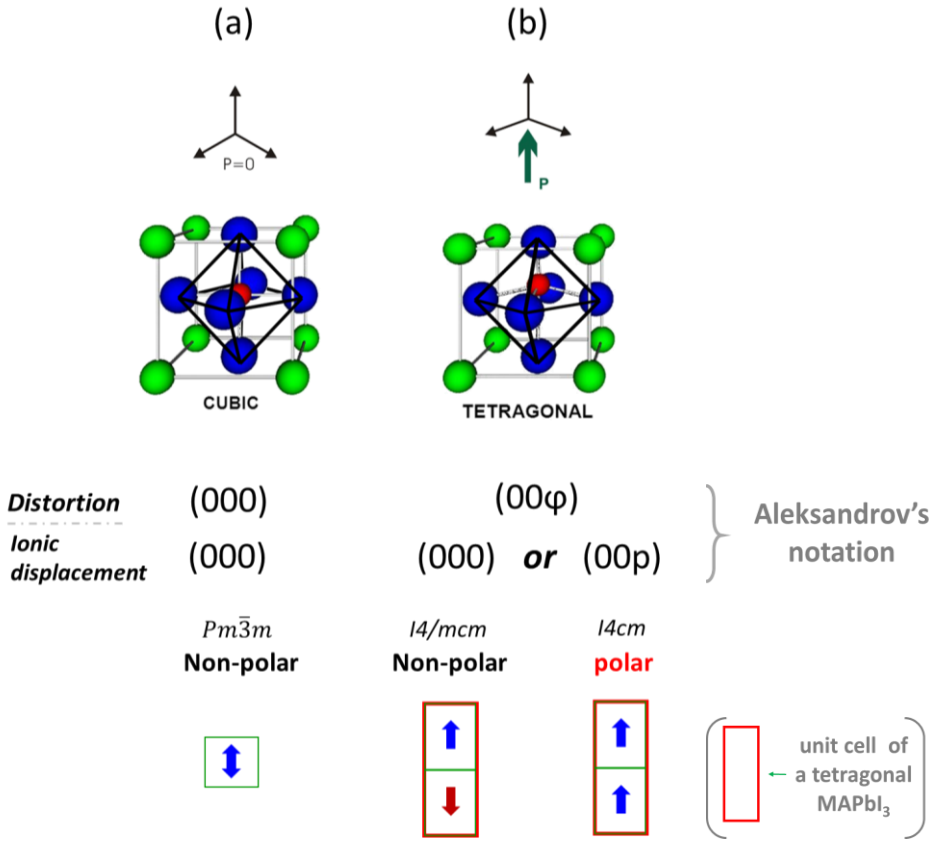

Fig. Si: Illustrations of the (a) cubic and (b) tetragonal phases relevant to the $MAPbI_3$ perovskite structure. The tetragonal symmetry can fit to two possible space groups that are very hard to distinguish, using diffraction methods. The difference will result in a material with a different dielectric nature.

Several methods can be used instead of diffraction methods, based on the relations between dielectric properties and bulk symmetry (see Fig. Sii), to get an idea about the symmetry-dictated dielectric nature of a material:

(1) *Polarization (P) vs. electric field (E)* scan hysteresis loops are the most direct evidence for ferroelectricity. As mentioned in the main text, high electrical conductivity and/or low stability will limit the interpretation of results using capacitance-based measurement systems, such as 'Sawyer Tower'-based methods (15).

(2) *Pyroelectricity*, will provide evidence for spontaneous polarization in the bulk material. Before concluding this, alternative explanations for a thermally stimulated electrical response (TSER) need to be excluded.

(3) Piezo-response force microscopy can give a partial understanding regarding the polar nature of the material('s surface). This technique can reveal ferro-*elasticity*(16) and piezoelectricity (17), which indicate a non-centrosymmetric space group of a material. However, the method, which has been quite popular in halide perovskite research, cannot directly determine the polar nature of the material.

(4) Second harmonic generation (SHG) will occur whenever a material lacks a centre inversion symmetry in at least one crystallographic direction, meaning that a material is non-centrosymmetric (18).

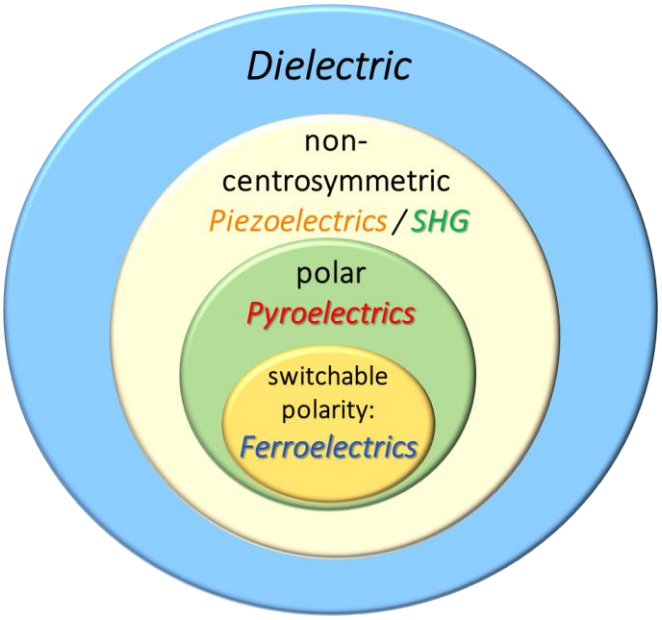

Fig. S ii: Schematic illustration of the progression from more general to more specific dielectric properties and techniques to identify them. For example, the scheme illustrates that if a material is ferroelectric it must be polar and non-centrosymmetric.

Section 2: *Pyroelectric current response and calculation of domain period, ω*:

The pyroelectric current, I_p, is given by the following relation (19):

S1) $$I_p = I_0 \cdot erf\left(\frac{\omega}{\sqrt{4 \cdot \delta \cdot t}}\right)$$

S2) $$I_0 = \frac{A \cdot F_d \cdot \alpha}{C_V \cdot (d + \omega)}$$

where ω is the size of the polar domain, δ [$cm^2 \cdot s^{-1}$] is the thermal diffusion coefficient, t [s] is the time of during the laser pulse, I_0 [A] is the current at $t = 0$, C_V [$J \cdot K^{-1} \cdot cm^{-3}$] is the thermal capacitance per unit volume, α [$C \cdot K^{-1} \cdot cm^{-2}$] is the pyroelectric coefficient, F_d [$W \cdot cm^{-2}$] is the heat flux at the surface, A [cm^2] the electrode area and d [cm] is the sample thickness. Since I_p depends on d and A, it is customary to present a normalized current, i_p, instead of I_p:

S3) $$i_p = \frac{d}{A} \cdot I_p .$$

From the pyroelectric current, we can estimate the polar domain size as follows. Using the *erf* table and equation S1 we can write that at half-maximum current (i=0.5i_0):

S4) $$\frac{\omega}{\sqrt{4 \cdot \delta \cdot t_{HM}}} = 0.48$$

where t_{HM} is the decay time from the maximum current to the half-maximum current after subtracting the system delay time (20 μs for our system). Now, if we assume that δ=*6*×10^{-3} $cm^2 \cdot s^{-1}$ for $MAPbI_3$ (20) and estimate from Fig. 4(b) that t_{HM}=140 sec, we find, using equation S2, ω ~ 9 μm.

Section 3: *Crystallographic identification from specular x-ray diffraction*

X-ray diffraction is performed in the Bragg-Brentano reflection geometry using a TTRAX III (Rigaku, Japan) a θ-θ diffractometer, equipped with a rotating Cu anode operating at 50 kV and 200 mA and with a scintillation detector aligned at the diffracted beam. For general crystallization product identification crystals were pulverized and powder diffraction of the resulting sample was performed. After confirming that the result conformed to the known diffractogram of $MAPbI_3$, the natively exposed faces of a crystal were aligned parallel to the specular plane of the scan to identify the {001} plane, which corresponds to the polar direction in *I4cm* symmetry. To distinguish between the slight differences of {001} and {110} crystallographic orientations, a high 2θ angle was scanned. This is done to allow diffraction from the well separated n=4 multiples of the (002) and (110) diffractions at 2θ=58.2° and 58.8°, respectively. As some crystals showed both diffractions (most likely due to twinning, which is very probable for tetragonal symmetry), we used further only crystals with highly oriented {001} planes for our studies. Fig. S1 shows an example of an actual diffraction result from different spontaneously exposed planes of an $MAPbI_3$ crystal.

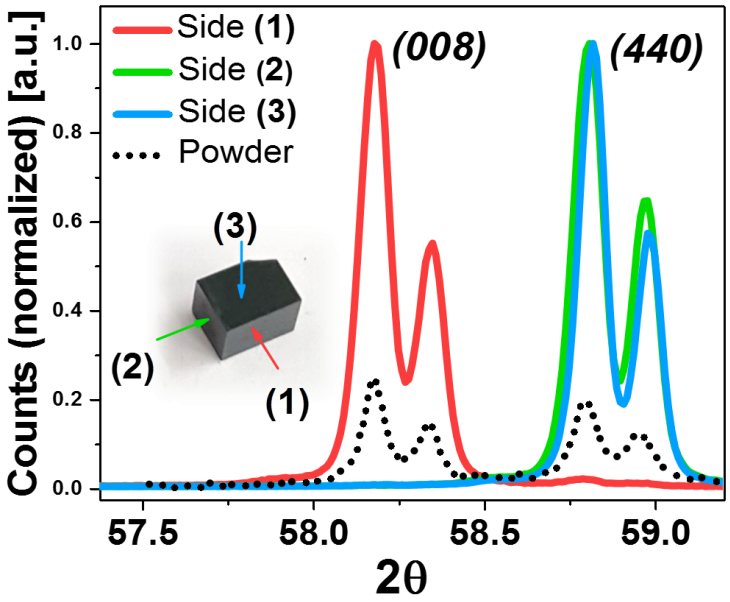

Fig. S 1: (a) Specular x-ray diffraction from crystal #3 (as shown in the inset). Three well-developed sides of the crystal were scanned after aligning the crystal face parallel to the specular plane. The 2θ angle was set to allow diffraction from the n=4 reflections of the (002) and (110) diffractions. We found that 'sides 1' corresponded to the {001} faces and the other two sides corresponded to the {110} faces, as expected from the tetragonal symmetry of $MAPbI_3$. The two adjacent peaks result from the Cu $K\alpha_1$ and $K\alpha_2$.

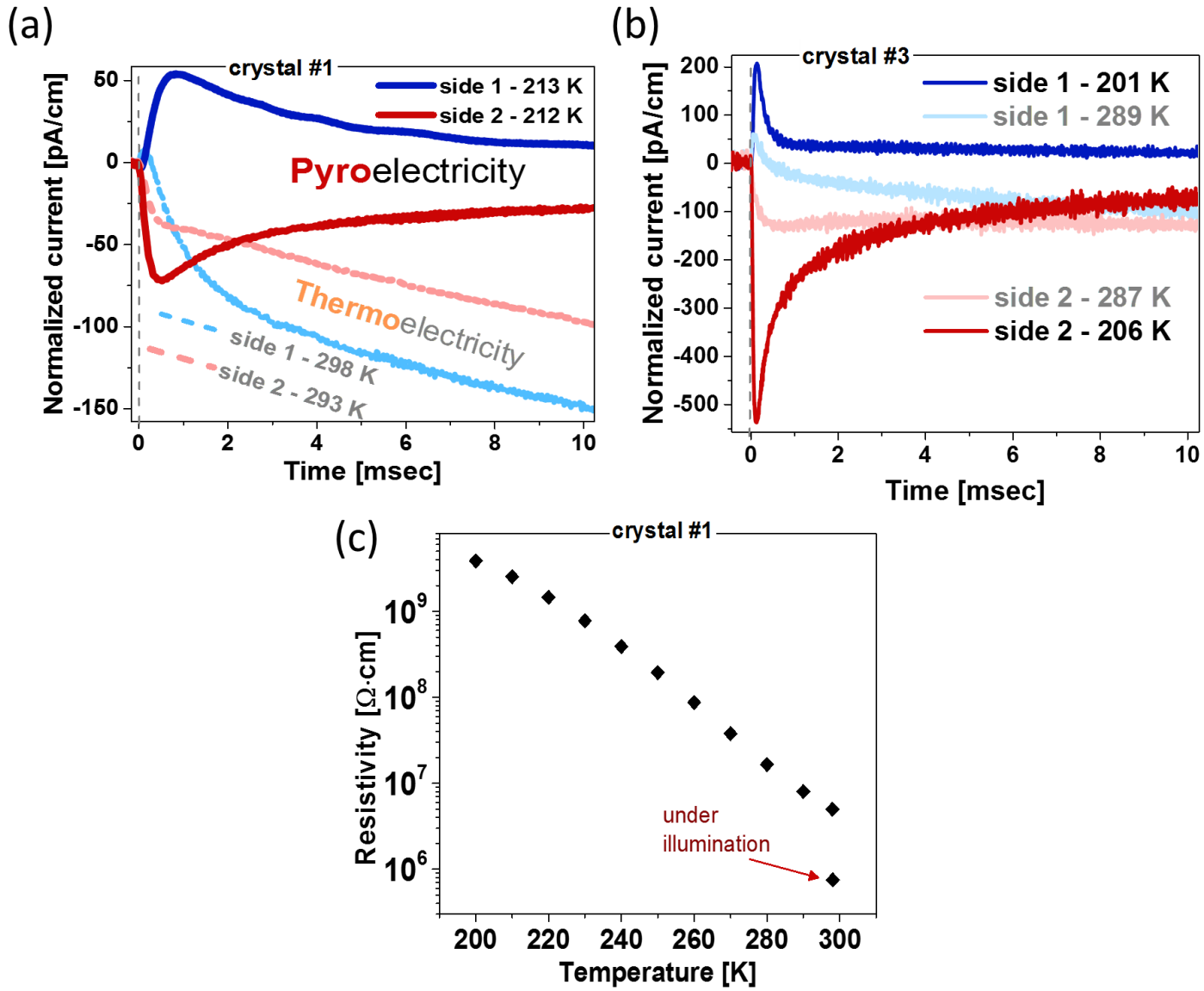

Fig. S 2: TSER response at *RT* (pale-colored plots) and *low* temperatures (deep-colored plots) of two crystals, in addition to the one, used for the results shown in Fig. 2 in the main text: (a) crystal #1: PbI_2:MAI molar ratio = 1:1; crystal morphology – hexagonal (diamond-like) prism. (b) Crystal #3: PbI_2:MAI molar ratio = 1:2; crystal morphology – rectangular prism. We used ethyl acetate as an anti-solvent for the growth of these two crystals. The polar nature of the PbI_2:MAI - 1:2 crystal is more pronounced, but is not absent in the 1:1 crystal. For crystal #2 (shown in the main text) we used diethyl ether as an anti-solvent and a PbI_2 to MAI ration of 1:2.

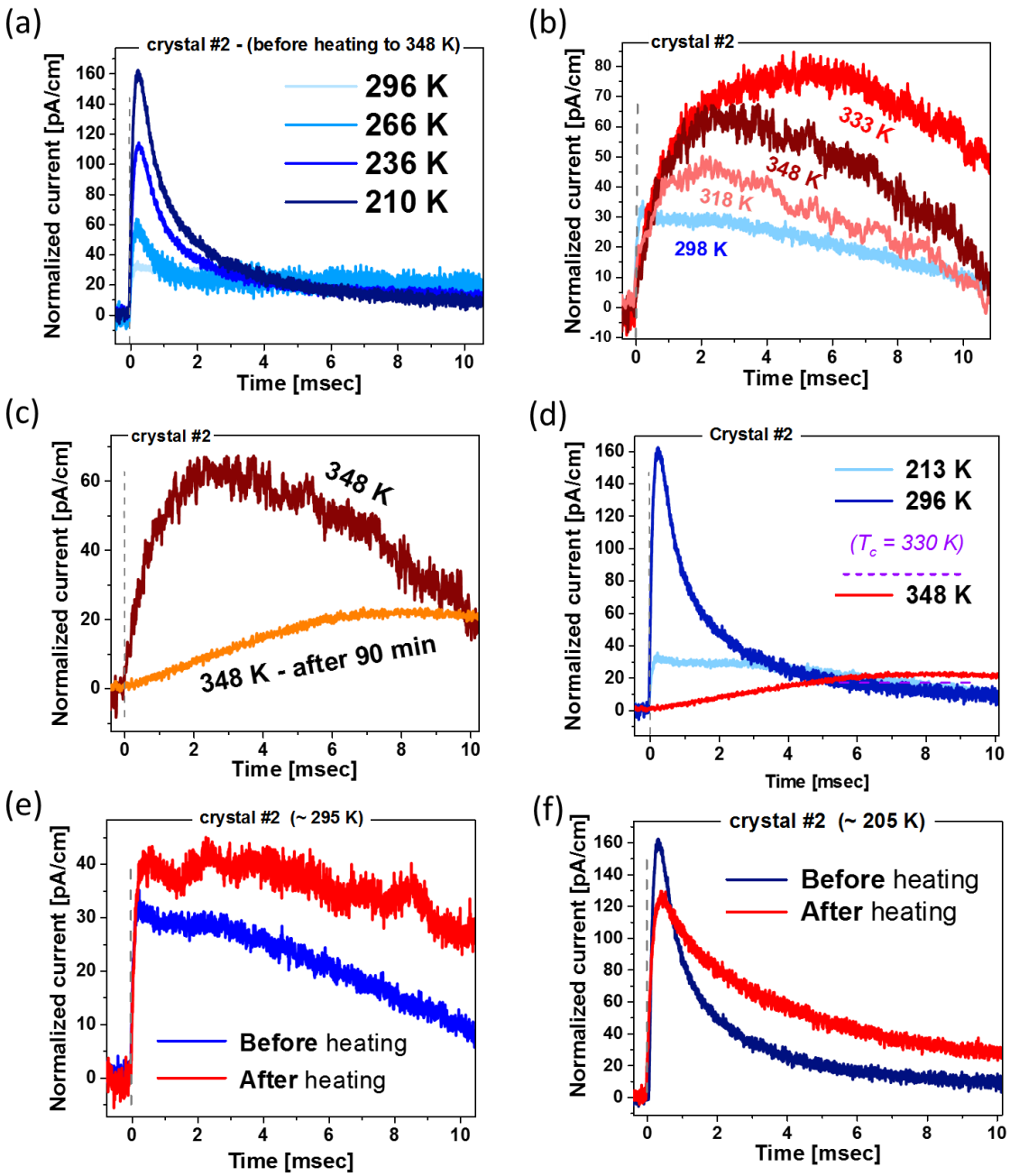

Fig. S 3: Thermally Stimulated Electric Response, TSER, dependence on environmental temperature as evidence for the pyroelectric nature of the TSER signal. (a) TSER upon cooling from *RT*; (b) TSER upon heating from *RT*; (c) TSER after 10 minutes and after 100 minutes from the moment the temperature reached 348 K; (d) comparison between the *low, RT* and high (>330 K) temperature TSER signals; (e) TSER at RT before and after heating to 348 K for 100 min; (d) TSER at *low* temperature before and after heating to 348 K for 100 min.

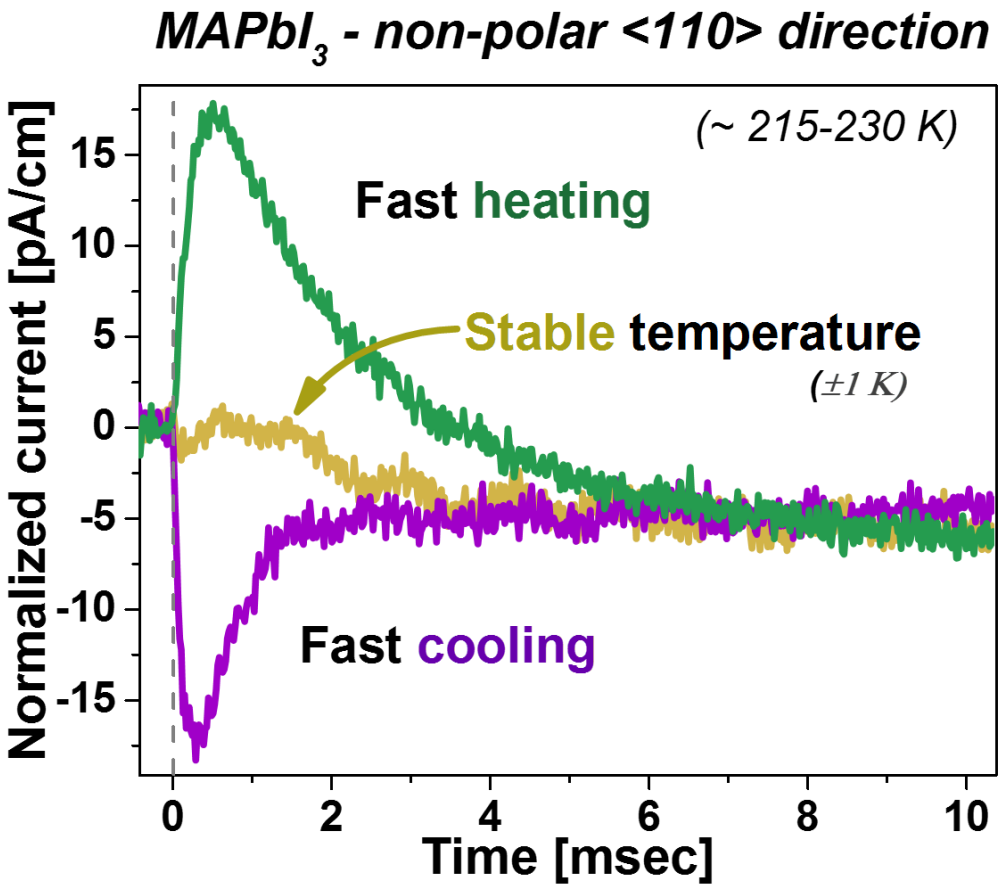

Fig. S 4: TSER at LT along the {110} plane of a $MAPbI_3$ crystal. Upon fast heating or cooling the peak current can be reversed, which strongly indicates these TSER signals are related to *flexoelectric* polarization (creation of dipole due to strong inhomogeneous thermal expansion along the crystal). If the temperature is stable (±1 K) the flexoelectric currents disappear and the small remaining current is, most likely, related to residual thermoelectric currents.

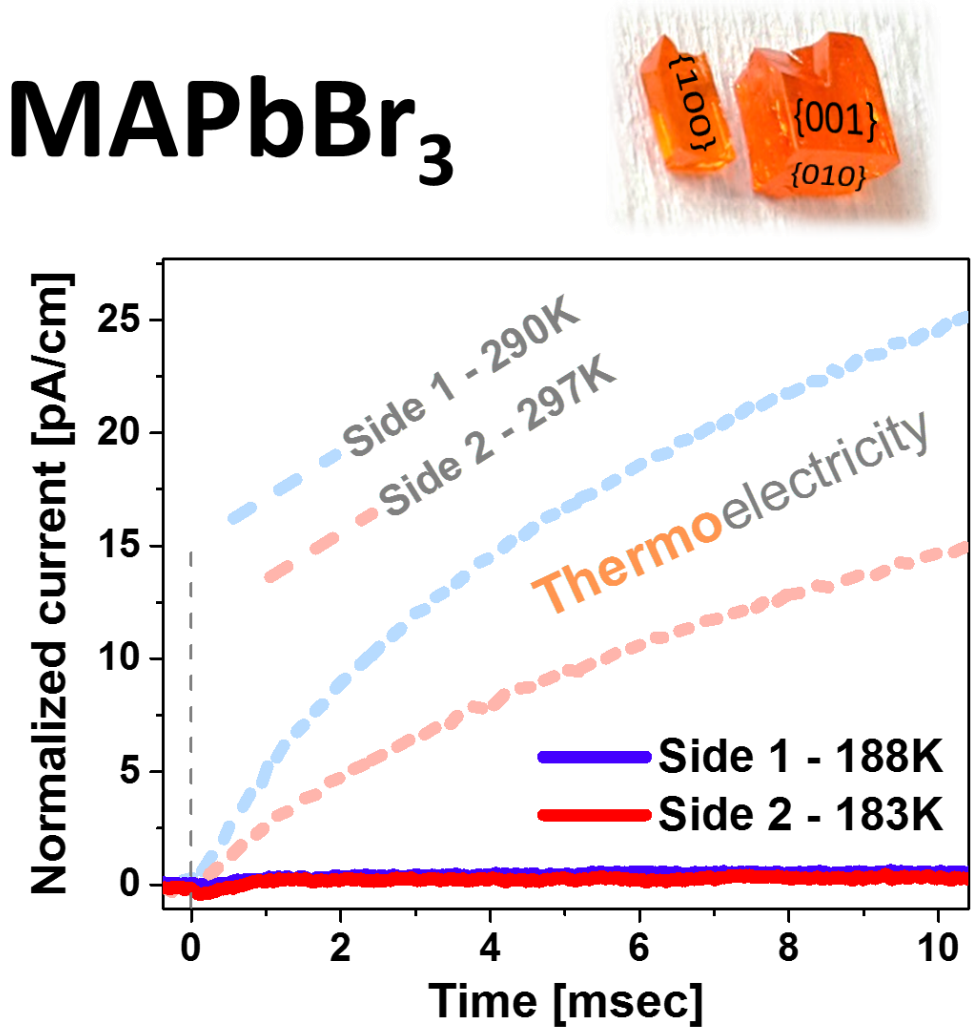

Fig. S 5: TSER of $MAPbBr_3$ along one of the {100} directions showing only thermoelectric currents (pale colored plots) and zero response at ~185 K deep-colored plots – a temperature well below its cubic to tetragonal phase transition temperature (@ 235 K and well above the tetragonal to orthorhombic one, 145 K). The opposite thermoelectric current sign of the $MAPbBr_3$ - positive - crystal to that of $MAPbI_3$ - negative – is explained by the different Fermi level position with respect to the valence and conduction bands: TSER indicates that $MAPbBr_3$ isa *p*-type and $MAPbI_3$ is *n*-type.

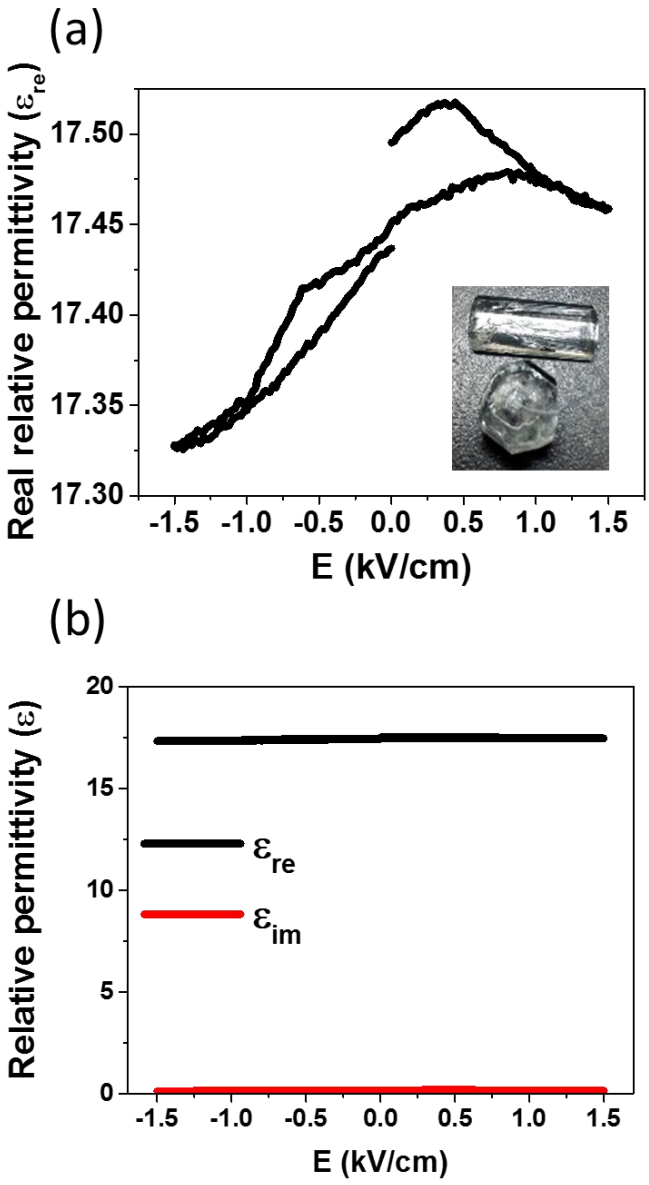

Fig. S 6: Dielectric response of a crystal of Rochelle salt (Potassium Sodium Tartrate, $KNa(OC(O)C(OH))_2 \cdot 4H_2O$) cleaved across its polar direction to a ~1 mm thick plate. The dielectric response is measured with an impedance analyzer (at 122 kHz and 1 V_{AC}) under a bias electric field (see experimental section, Fig. 1(d)). The measuring temperature was 273 K, where the polarization response to a bias electric field, E_{DC} is maximal.(15) (a) The real part of the relative permittivity, ε_{re}, as function of E_{DC}. The change in the dielectric response is small (fraction of a percent), but still shows a very similar profile to that of $Pb(Zr_xTi_{1-x})O_3$, PZT, in which the change in dielectric response can be more than 100% (22). (b) Comparison of the real, ε_{re}, and the imaginary (lossy) part, ε_{im}, of the relative permittivity. It is clearly seen that ε_{im} can be neglected for this material.

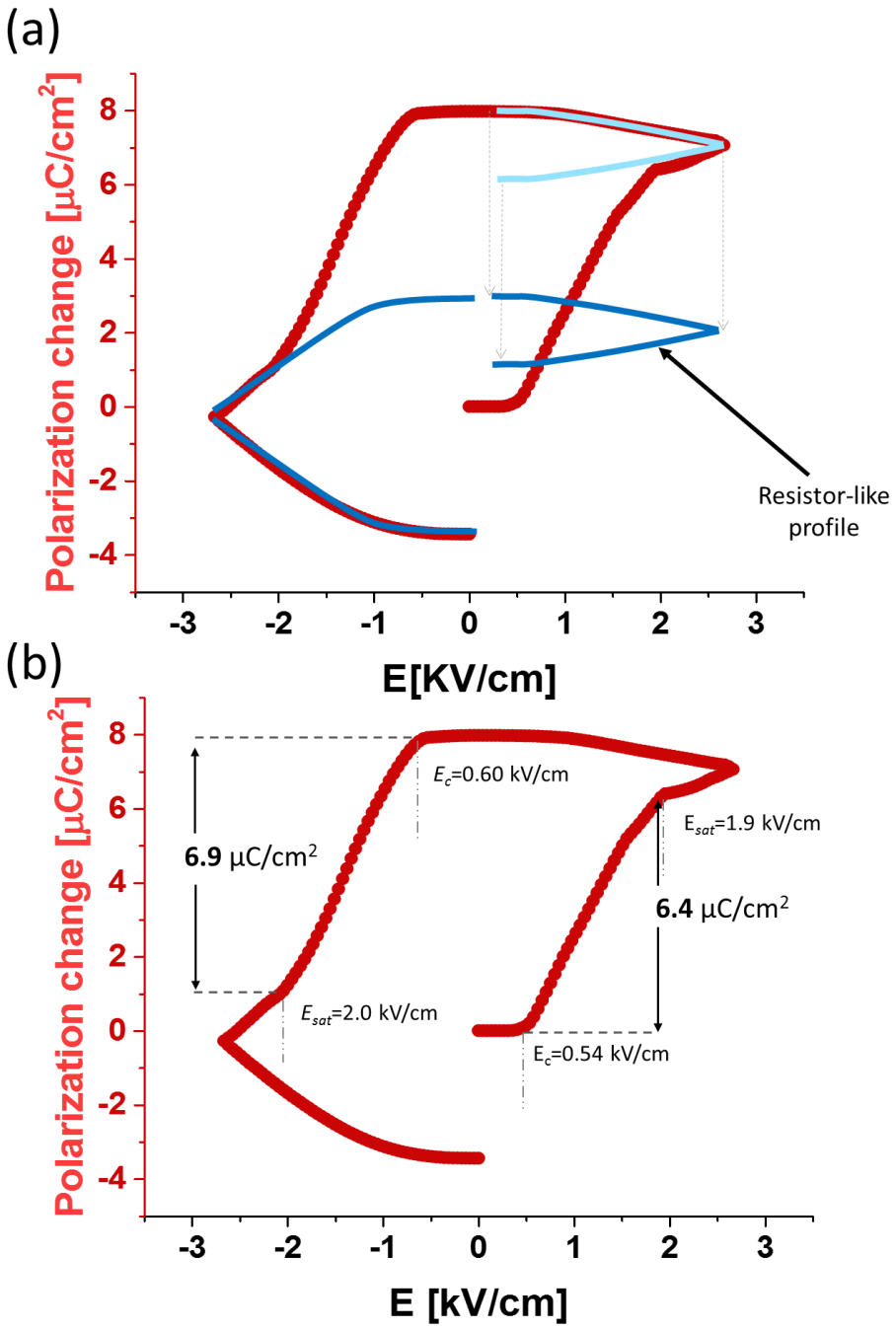

Fig. S 7: (a) Qualitative deconvolution of the hysteresis loop, shown in Fig. 3(b) illustrating that the loop is composed of a lossy part (*i.e.*, resistor-like polarization; blue) and a ferroelectric part (sharp transitions due to ferroelectric polarization). (b) Analysis of the ferroelectric polarization part. The average between the positive and negative bias of the coercive field (E_c), saturation field (E_{sat}) and saturation change in polarization (P_{sat}) show similar values on both the positive and negative parts of the loop, indicating true ferroelectric switching. The positive and the negative sides of the loop are not equivalent due to asymmetric contacts or some irreversible degradation due to the high applied electric field.

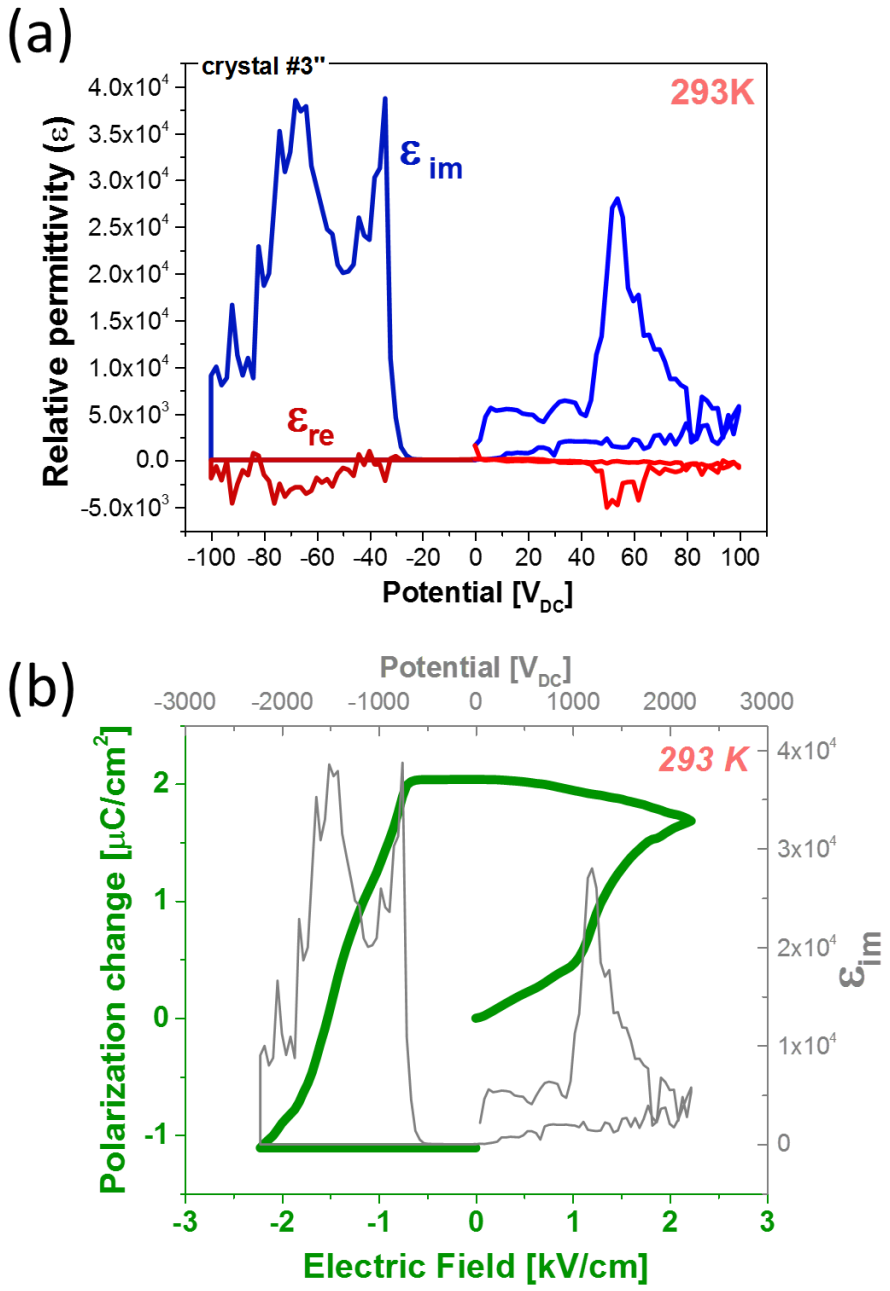

Fig. S 8: (a) Dielectric response at RT of a $MAPbI_3$ crystals along its <001> direction 2222 Hz (V_{AC} =0.1 V) as a function of an applied bias, E_{DC}. The ε_{im}-E_{DC} scan was done after the scan at LT. Similarly, to the response at LT, the RT response shows a dominant imaginary (lossy) part of the dielectric response. (b) P-E hysteresis loop obtained from integration of ε_{im} over E_{DC} (see Eq. 1). The greater (negative) values in ε_{re} can be related to electrochemical irreversible degradation due to the applied electric field (and voltage), that eventually cause severe damage to the sample (see lower left part of the loop). This degradation does not allow a fair analysis of the loop (positive part - before the severe damage) as ferroelectric switching.

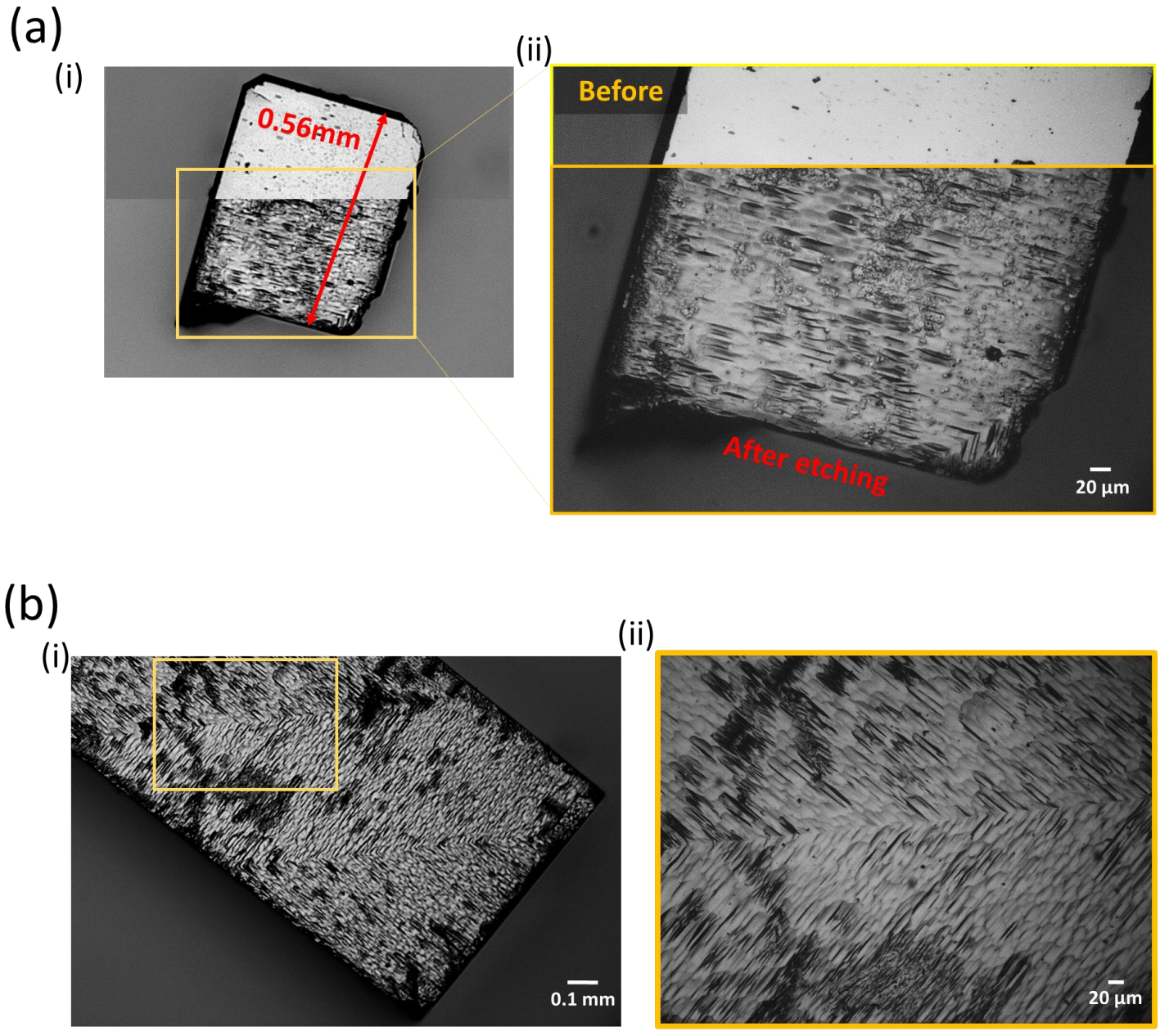

Fig. S 9: Bright field image from a light microscope of a crystal before and after etching in acetone for 120 sec. (a) and (b) are crystals grown in a 1:1 PbI_2 to MAI solution using diethyl ether as an anti-solvent. (a) is found to be a single crystal while (b) is a crystal with two twin boundaries. At such a twin boundary the polar domains are orthogonal to each other. (ii) are magnified view of the yellow rectangles marked in (i).

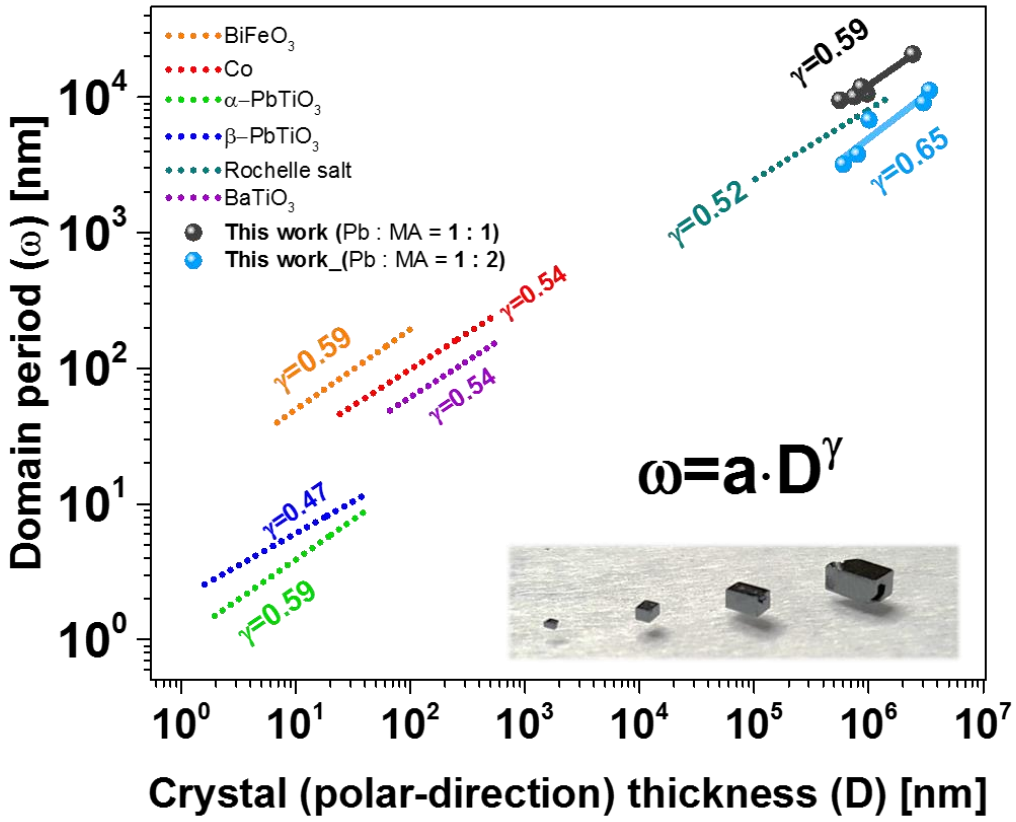

Fig. S 10: Domain periodicity with respect to the crystal thickness in the polar direction. The data are an average obtained from several microscope images after etching in acetone for ~120 sec. The values of γ are obtained by fitting to a $\omega = a \cdot D^{\gamma}$ function. The fitted lines for the other ferroic materials are taken from refs. (23, 24). These are introduced to compare with our results, showing good agreement with the global scaling law between bulk sample dimensions and domain periodicity.

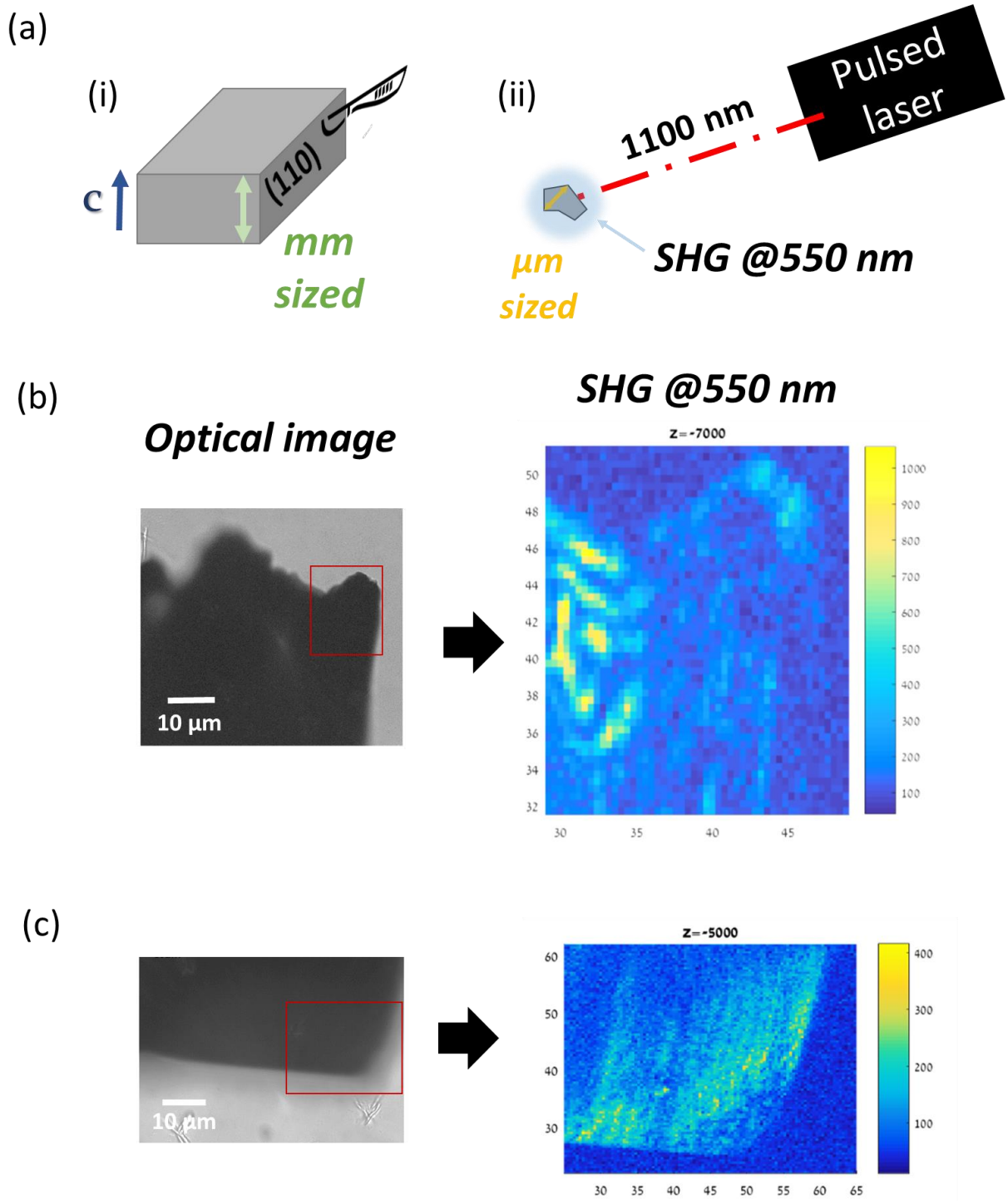

Fig. S 11: (a) I illustration of (i) the way a sample was prepared for the SHG detection experiment and (ii) its measurement. (b) and (c) are examples of results from different pieces of such samples (*cf.* also Fig. 6 in main text).

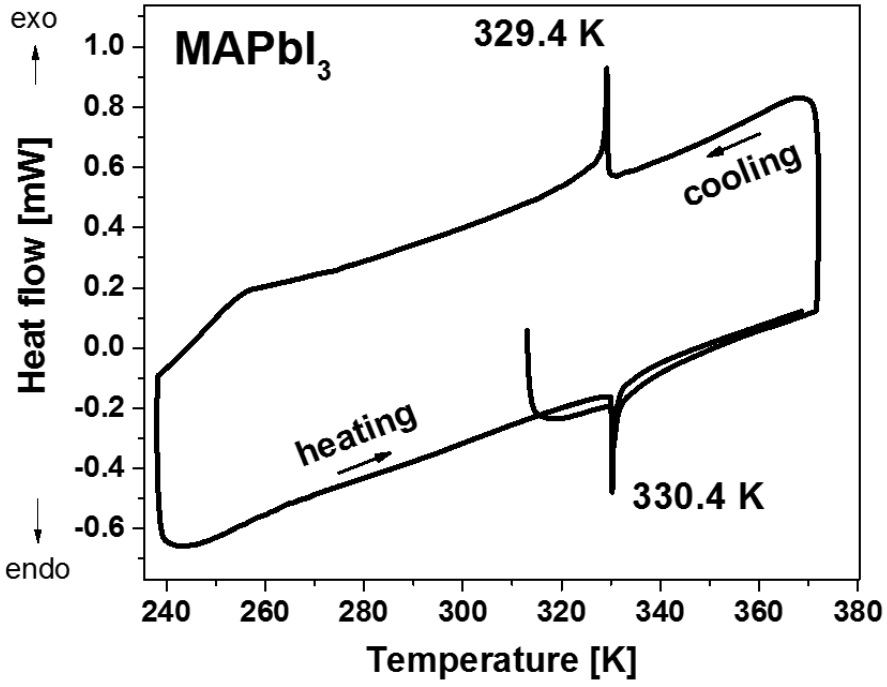

Fig. S 12: Differential scanning calorimetry (DSC) of 0.3-1 mm crystals grown below the tetragonal-to-cubic phase transition as described in the experimental section. DSC was carried in a Q200 model from "TA instruments" using hermetically sealed aluminum pans under N_2 flow at a heating rate of 10 °C/min and cooling rate of 5 °C/min.

References

1. Goldschmidt VM (1926) Die Gesetze der Krystallochemie. *Naturwissenschaften* 14(21):477–485.

2. Glazer AM (1972) The classification of tilted octahedra in perovskites. *Acta Crystallogr B* 28(11):3384–3392.

3. Thomas NW (1998) A New Global Parameterization of Perovskite Structures. *Acta Crystallogr B* 54(5):585–599.

4. Aleksandrov KS (1978) Mechanisms of the ferroelectric and structural phase transitions. structural distortions in perovskites. *Ferroelectrics* 20(1):61–67.

5. Aleksandrov KS, BartolomÉ J (2001) Structural distortions in families of perovskite-like crystals. *Phase Transit* 74(3):255–335.

6. Cohen RE (1992) Origin of ferroelectricity in perovskite oxides. *Nature* 358(6382):136–138.

7. Frost JM, et al. (2014) Atomistic Origins of High-Performance in Hybrid Halide Perovskite Solar Cells. *Nano Lett* 14(5):2584–2590.

8. Liu S, et al. (2015) Ferroelectric Domain Wall Induced Band Gap Reduction and Charge Separation in Organometal Halide Perovskites. *J Phys Chem Lett* 6(4):693–699.

9. Mashiyama H, et al. (2007) Disordered Configuration of Methylammonium of CH3NH3PbBr3 Determined by Single Crystal Neutron Diffractometry. *Ferroelectrics* 348(1):182–186.

10. Weller MT, Weber OJ, Henry PF, Pumpo AMD, Hansen TC (2015) Complete structure and cation orientation in the perovskite photovoltaic methylammonium lead iodide between 100 and 352 K. *Chem Commun* 51(20):4180–4183.

11. Whitfield PS, et al. (2016) Structures, Phase Transitions and Tricritical Behavior of the Hybrid Perovskite Methyl Ammonium Lead Iodide. *Sci Rep* 6:35685.

12. G S, et al. (2016) Is $CH_3NH_3PbI_3$ Polar? *J Phys Chem Lett* 7(13):2412–2419.

13. Hallstedt B, Risold D, Gauckler LJ (1997) Thermodynamic Assessment of the Bismuth–Strontium–Oxygen Oxide System. *J Am Ceram Soc* 80(5):1085–1094.

14. Barnes PW (2003) Exploring structural changes and distortions in quaternary perovskites and defect pyrochlores using powder diffraction techniques. Dissertation (The Ohio State University). Available at: https://etd.ohiolink.edu/pg_10?0::NO:10:P10_ACCESSION_NUM:osu1064346592.

15. Sawyer CB, Tower CH (1930) Rochelle Salt as a Dielectric. *Phys Rev* 35(3):269–273.

16. Hermes IM, et al. (2016) Ferroelastic Fingerprints in Methylammonium Lead Iodide Perovskite. *J Phys Chem C* 120(10):5724–5731.

17. Kim Y-J, et al. (2016) Piezoelectric properties of $CH_3NH_3PbI_3$ perovskite thin films and their applications in piezoelectric generators. *J Mater Chem A* 4(3):756–763.

18. Boyd RW (2008) *Nonlinear optics* (Elsevier/Academic Press, Amsterdam). 3. ed.

19. Ehre D, Mirzadeh E, Stafsudd O, Lubomirsky I (2014) Pyroelectric Measurement of Surface Layer: The Case of Thin Film on Dielectric Substrate. *Ferroelectrics* 472(1):41–49.

20. Qian X, Gu X, Yang R (2016) Lattice thermal conductivity of organic-inorganic hybrid perovskite $CH_3NH_3PbI_3$. *Appl Phys Lett* 108(6):063902.

21. Damjanovic D (1998) Ferroelectric, dielectric and piezoelectric properties of ferroelectric thin films and ceramics. *Rep Prog Phys* 61(9):1267.

22. Placeres-Jiménez R, Rino JP, Eiras JA (2015) Modeling ferroelectric permittivity dependence on electric field and estimation of the intrinsic and extrinsic contributions. *J Phys Appl Phys* 48(3):035304.

23. Catalan G, Scott JF, Schilling A, Gregg JM (2007) Wall thickness dependence of the scaling law for ferroic stripe domains. *J Phys Condens Matter* 19(2):022201.

24. Catalan G, et al. (2008) Fractal Dimension and Size Scaling of Domains in Thin Films of Multiferroic BiFeO3. *Phys Rev Lett* 100(2):027602.